Highly-directive Cross-polarized Backscatterers Integrated with a Ground Plane

Osmery Hernández, Iban Buldain, Iñigo Ederra, Richard W. Ziolkowski, *Life Fellow, IEEE* and Iñigo Liberal, *Member, IEEE*

Abstract—**Cross-polarized backscatterers integrated with a ground plane are a key element of different applications including chipless RFIDs, sensing, ambient backscattering communications and data-storage. The use of a cross-polarized signal removes the difficulties arising from the strong co-polar signal reflected by the ground plane. Concurrently, the cross-polarized signal is typically very weak, hindering the effectiveness of cross-polarized backscatterers in noisy and uncontrolled environments. Herein, the generalized optical theorem is used to derive upper bounds on the cross-polarized backscattering cross-section of systems integrated with a ground plane and to identify viable strategies to design them based on highly-directive scattering systems. Popular antenna configurations, including elementary electric and magnetic dipoles and their combinations as Huygens sources and end-fire arrays, are examined to ascertain which ones can be used to realize highly-directive cross-polarized backscattering performance when they are integrated with a ground plane. Realistic single antenna elements that attain the upper-bound performance are identified. A two-element end-fire array based on crossed electric dipole elements also achieves the upper-bound performance, further confirming the efficacy of the derived cross-polarized backscattering bounds.**

Index Terms—**Antenna arrays, chipless RFIDs, radio frequency identification device (RFID), RFID mounted on metal, superdirectivity**

I. INTRODUCTION

SIMILAR to conventional antennas, the integration of low-profile and electrically small scattering systems with a ground plane are of interest for several technologies including chipless radio-frequency identification devices (RFIDs) [1]–[5], sensing [6]–[9], ambient backscattering communications [10]–[12] and optical data storage [13]. Typically, the presence of the ground plane is imposed by technological and application specific constraints such as the structure on which the system must be supported and/or the need of electromagnetically isolating its radiating and scattering parts from the rest of the system, e.g., a device mounted on a metallic body such as an automobile, drone or aircraft. However, the presence of a ground plane critically modifies the distribution of the fields radiated by local currents excited (induced) on it and the radiator/scatterer by some internal (external) excitation. Therefore, the design of both antennas and scatterers integrated

O. Hernández, I. Buldain, I. Ederra and I. Liberal are with the Department of Electrical, Electronic and Communications Engineering,Public University of Navarra, 31006 Pamplona, Spain.

I. Ederra and I. Liberal are with the Institute of Smart Cities, Public University of Navarra, 31006 Pamplona, Spain

R.W. Ziolkowski is with the Global Big Data Technologies Centre, University of Technology Sydney, Ultimo NSW 2007, Australia

Corresponding author: I. Liberal (email: inigo.liberal@unavarra.es)

with a ground plane must be specialized to account for its influence.

Previous designs of backscatterers integrated with a ground plane have been heavily inspired by antenna theory, with their geometry consisting of dipoles [5], [7], concentric rectangular loops [2]–[4], [6], microstrip patches [14] and a variety of metamaterial-inspired constructs. Cross-polarized backscatterers are of particular interest as they enable the isolation of the signal of interest from the co-polarized ground plane reflection. In fact, the strong echo from a large metallic body severely limits the read range and the frequency selectivity of the co-polar component of the back scattered signal as the size of the ground plane increases [2]. On the other hand, the main drawback of using the cross-polarized component of the backscattered signal is its even smaller strength, typically being several orders of magnitude weaker than the total co-polar field which includes not only the scattered co-polarized signal, but also the reflection of the incident field from the ground plane. This feature of a cross-polarized scattered signal hinders its implementation in noisy and uncontrolled environments, e.g., in industrial and/or outdoor situations.

The maximization of the power scattered by an electrically small system is a central topic of electromagnetic theory for which several theoretical bounds and optimization procedures have been actively investigated [15]–[24]. This fact suggests that basic electromagnetic scattering theory could be applied to identify optimal design strategies for cross-polarized backscatterers integrated with a ground plane. For instance, the optical theorem was used in a previous work [17] to derive upper bounds of different scattering processes, i.e., the total scattering, total absorption, minimum scattering and bistatic scattering. Those previous studies showed that all of these scattering processes are upper bounded by the scattering directivity of the object back into the direction of the source of the incident field. These upper bounds result from the constraints imposed by the need for an efficient extraction of energy from the incident field through destructive interference. This conclusion revealed that highly directive systems are beneficial for most scattering processes, and it provided design guidelines for the development of a variety of devices. For example, this theory was applied to design superbackscattering systems consisting of arrays of antennas [25], dielectric resonators [26] and nanoparticles dimers [27] whose backscattering cross sections approach the theoretical upper bounds.

Here, we extend our previous results to the case of a scattering system integrated with a ground plane under arbitrary far-

field illumination, and we use this theory to provide guidelines for the design of optimized cross-polarized backscatterers. To this end, the remainder of the manuscript is organized as follows. First, Section II introduces the general theory and notations for the analysis of scattering systems integrated with a ground plane. This approach is particularized in Section III to the technologically relevant case of specular cross-polarized backscatterers. We then revisit the performance that can be obtained with popular highly-directive systems, including electric and magnetic Hertzian dipoles, as well as their combinations into Huygens sources and end-fire arrays. Finally, our concluding remarks are established in Section IV.

We note that while other design and analysis techniques could be applied to the same problem, e.g., a full-fledged numerical optimization, the developed theory highlights the key role that directivity plays in optimizing the scattering processes. Moreover, it provides important, innovative physical insights into the limiting factors on this class of electromagnetic field-matter interactions. Furthermore, it suggests practical design guidelines. An in depth study of the performance that can be expected from known antenna and scattering systems, such as elementary dipoles, Huygen's sources and end-fire arrays, in the presence of a ground plane is given. Nonetheless, numerical parameter studies of example symmetric and asymmetric backscatterers are used to confirm these theoretical developments.

II. GENERAL THEORY FOR SCATTERING SYSTEMS INTEGRATED WITH A GROUND PLANE

We start by considering the geometry schematically depicted in Fig. 1, where a scatterer is placed near to a ground plane whose exterior surface corresponds to the XY plane. The scatterer is defined as a local permittivity distribution $\varepsilon(\mathbf{r})$. The electric field solution to this electromagnetic problem can be written as the superposition of the background and scattered fields [28]: $\mathbf{E}(\mathbf{r}) = \mathbf{E}^b(\mathbf{r}) + \mathbf{E}^s(\mathbf{r})$. The background field $\mathbf{E}^b(\mathbf{r})$ corresponds to the solution to Maxwell equations in the absence of the scatterer. It is composed of the incident fields radiated by the sources illuminating the system, as well as the reflections of those waves from the ground plane. On the other hand, the scattered field $\mathbf{E}^s(\mathbf{r})$ is defined as the fields radiated by the polarization currents induced in the scatterer. The time harmonic convention $e^{j\omega t}$ is assumed for all currents and fields and is omitted throughout.

Without loss of generality, we can apply a spatial Fourier transform taking Z as the preferred axis, and rewrite the background field as a superposition of plane waves [29]

$$\mathbf{E}^b(\mathbf{r}) = \sum_{\xi=I,R} \sum_{q=1,2} \int d^2k_\parallel \, \widehat{\mathbf{e}}_q(\mathbf{k}_\xi) E_{\xi q}(\mathbf{k}_\xi) e^{-j\mathbf{k}_\xi \cdot \mathbf{r}} \quad (1)$$

The spatial spectrum amplitude $E_{\xi q}(\mathbf{k}_\xi)$ has units [V-m]. We assume that the system is illuminated only by far-field sources. Thus, the integral in (1) only runs over propagating waves with the wave vectors $\mathbf{k}_I = \mathbf{k}_\parallel + \widehat{\mathbf{z}}\, k_z$ and $\mathbf{k}_R = \mathbf{k}_\parallel - \widehat{\mathbf{z}}\, k_z$ corresponding to the incident waves and the waves reflected by the ground plane, respectively. The term $\mathbf{k}_\parallel = \widehat{\mathbf{x}}\, k_x + \widehat{\mathbf{y}}\, k_y$ is the wavevector component parallel to
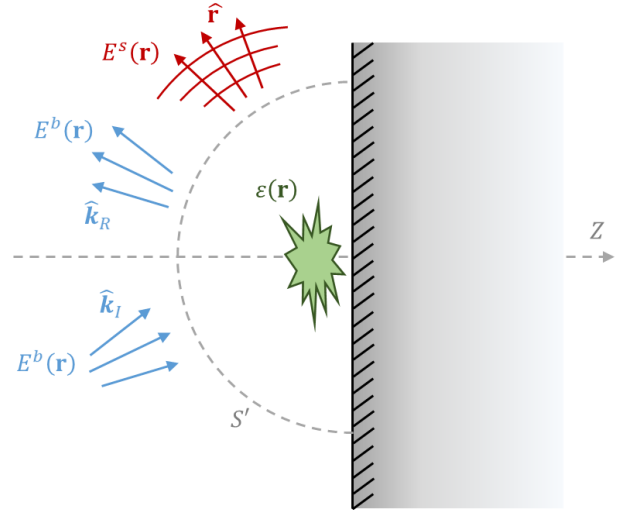

Fig. 1. Geometry of a scattering device, modeled as a permittivity distribution $\varepsilon(\mathbf{r})$, located near to the top surface of a ground plane. The total field is given by the superposition of the background and scattered fields, $\mathbf{E}(\mathbf{r}) = \mathbf{E}^b(\mathbf{r}) + \mathbf{E}^s(\mathbf{r})$. The background field $\mathbf{E}^b(\mathbf{r})$ consists of the solution to Maxwell equations in the absence of the scatterer, and thus it is given by the incident field radiated by the sources illuminating the system, and the reflection of those waves in the ground plane. The scattered field $\mathbf{E}^s(\mathbf{r})$ is the field radiated by the polarization currents induced in the device into multiple $\widehat{\mathbf{r}}$ directions.

the ground plane. The term $k_z \in \mathbb{R}^+$ is the component of the wavevector along the normal to the ground plane; it is a real and positive quantity for propagating waves. The sum also runs over the two possible transverse polarizations for a propagating plane wave, $\widehat{\mathbf{e}}_q(\mathbf{k}_\xi)$, with $q = 1, 2$. $E_{\xi q}(\mathbf{k}_\xi)$ is the amplitude of the electric field for each wavevector/polarization pair.

A common figure of merit that describes the scattering process is the power extracted by the scatterer from the background field. It equals the addition of the scattered and absorbed powers, $P_{\text{ext}} = P_{\text{abs}} + P_{\text{scat}}$ and can be written as a surface integral over the cross-terms of the Poynting vector field [30]. Asymptotically evaluating this integral by means of Jones' Lemma [31] leads to an expression for the extracted power similar to previous generalizations of the optical theorem in the presence of an interface [32], [33]:

$$P_{\text{ext}} = \frac{2\pi}{\omega\mu_0} \sum_{q=1,2} \text{Im} \int d^2k_\parallel \, E_{Rq}(\mathbf{k}_R) \widehat{\mathbf{e}}_q^*(\mathbf{k}_R) \cdot \mathbf{F}\left(\widehat{\mathbf{k}}_R\right) \tag{2}$$

where $\mathbf{F}(\widehat{\mathbf{r}})$ is the pattern of the scattered field in the far-field limit, i.e., $\mathbf{E}^s(\mathbf{r}) \longrightarrow \mathbf{F}(\widehat{\mathbf{r}}) e^{-jkr}/r$ as $r \to \infty$. Since $2\pi/(\omega\mu) = \lambda/\eta_0$, where η_0 is the wave impedance of free-space, the vector pattern $\mathbf{F}(\widehat{\mathbf{r}})$ thus has the units [V].

The optical theorem, given by Eq. (2), emphasizes the role of the destructive interference in the extraction process. In order to extract energy, the scattered field must have a nonzero projection on the direction and polarization of the background field, i.e., $\widehat{\mathbf{e}}_q^*(\mathbf{k}_R) \cdot \mathbf{F}(\widehat{\mathbf{k}}_R) \neq 0$. Since the scatterer can only produce outgoing waves and it lies near to the ground plane, only reflected waves contribute to Eq. (2). Importantly, the generation of the scattered far-fields must necessarily result

in radiation damping on the polarization currents. Therefore, highly-directive backscattering systems must radiate scattered fields that project onto the background field to provide a superior performance in any scattering process as measured by the total scattering, absorption, directional scattering, maximum/minimum scattering, ... In other words, a highly efficient scatterer must only radiate wavevector/polarization pairs that contribute to the extraction of energy, while avoiding those pairs that lose power to unwanted channels. This physical intuition can be mathematically justified by deriving inequalitites from Eq. (2).

First, we note that if f_m is a set of complex numbers, then $\sum_m \text{Im}(f_m) \leq \sum_m |f_m|$. Consequently, the following inequality for the extracted power follows immediately from Eq. (2):

$$P_{\text{ext}} \leq \frac{2\pi}{\omega\mu_0} \sum_{q=1,2} d^2 k_\parallel E_{Rq}(\mathbf{k}_R) \left| \widehat{\mathbf{e}}_q^*(\mathbf{k}_R) \cdot \mathbf{F}\left(\widehat{\mathbf{k}}_R\right) \right| \quad (3)$$

Next, we recall that the definition of the scattering directivity into each polarization state is given by the relation [34]:

$$D_{\text{scat}}(\widehat{\mathbf{r}}, q) = 4\pi \frac{1}{2\eta_0} \frac{|\widehat{\mathbf{e}}_q(\widehat{\mathbf{r}}) \cdot \mathbf{F}(\widehat{\mathbf{r}})|^2}{P_{\text{scat}}} \quad (4)$$

Thus, the inequality (3) can then be rewritten using (4) as follows:

$$P_{\text{ext}} \leq \frac{2\pi}{\omega\mu_0} \sum_{q=1,2} \int d^2 k_\parallel E_{Rq}(\mathbf{k}_R) \sqrt{\frac{2\eta_0 P_{\text{scat}} D_{\text{scat}}\left(\widehat{\mathbf{k}}_R, q\right)}{4\pi}}$$

$$\leq \frac{\lambda}{\sqrt{2\pi\eta_0}} \sqrt{P_{\text{scat}}} \sum_{q=1,2} \int d^2 k_\parallel E_{Rq}(\mathbf{k}_R) \sqrt{D_{\text{scat}}\left(\widehat{\mathbf{k}}_R, q\right)}$$
$$(5)$$

Finally, by introducing the projection factor

$$P_B = \frac{\lambda^2}{2\pi\eta_0} \left[\sum_{q=1,2} \int d^2 k_\parallel E_{Rq}(\mathbf{k}_R) \sqrt{D_{\text{scat}}\left(\widehat{\mathbf{k}}_R, q\right)} \right]^2 \quad (6)$$

the inequality given by (5) can be compactly written as:

$$P_{\text{ext}} = P_{\text{scat}} + P_{\text{abs}} \leq \sqrt{P_{\text{scat}} P_B} \quad (7)$$

The projection factor, P_B, is the power that describes the scattering directivity weighted over the directions and polarizations of the background field. It is a figure of merit that determines how efficiently the scattered field is projected onto the background field. As a result, the P_B factor is critical to the determination of the performance of different scattering systems.

We note that Eq. (7) is mathematically equivalent to the inequality derived in [17] for the case of scatterers standing in free-space and illuminated by a single plane-wave. The only difference is that the background power factor P_B becomes

an integral over the multiple reflection directions and polarizations, instead of the simple forward scattering directivity. Due to this mathematical equivalence, the methods employed in [17] were readily adopted here for the derivation of the upper bounds in this more general case. For example, upper bounds for the total scattered and absorbed powers can be found by maximizing the different terms in Eq. (7). In particular, the scattered power is maximized in the lossless limit, $P_{\text{abs}} = 0$, and its upper-bound is $P_{\text{scat}} \leq P_B$. On the other hand, the absorbed power is maximized when $P_{\text{abs}} = P_{\text{scat}}$, and its upper bound is $P_{\text{abs}} \leq (1/4) P_B$.

The performance of minimum scattering antennas (or cloaked sensors) is usually defined by their absorption efficiency [34]: $\eta_{\text{abs}} = P_{\text{abs}}/(P_{\text{scat}} + P_{\text{abs}})$. With this definition one has $\eta_{\text{abs}}(1 - \eta_{\text{abs}}) = P_{\text{abs}} P_{\text{scat}}/(P_{\text{scat}} + P_{\text{abs}})^2$ and Eq. (7) then yields $P_{\text{abs}} \leq \eta_{\text{abs}}(1 - \eta_{\text{abs}}) P_B$, illustrating the maximum absorption that can be obtained for a given level of absorption efficiency η_{abs}. Again, its upper bound $P_B/4$ is attained when $\eta_{\text{abs}} = 1/2$. Similarly, the power scattered into a given direction and polarization pair is given by $\mathcal{P}(\widehat{\mathbf{r}}, q) = P_{\text{scat}} D_{\text{scat}}(\widehat{\mathbf{r}}, q)$, with the upper bound $\mathcal{P}(\widehat{\mathbf{r}}, q) \leq D_{\text{scat}}(\widehat{\mathbf{r}}, q) P_B$.

This set of upper bounds is a generalization of our work in [17] which was restricted to scattering systems located in free-space and under single plane-wave illumination. It reveals that the performance of any scattering system (absorption, total scattering, minimum scattering antennas and directional scattering) located on a ground plane and under arbitrary far-field illumination critically depends on how precisely the scattered far-field projects onto the background field. Therefore, the performance of the system is ultimately limited by the scattering directivity.

III. HIGHLY-DIRECTIVE CROSS-POLARIZED BACKSCATTERERS

These general scattering theory results are applied now to the case of specular cross-polarized backscatterers. A sketch of this particular scattering process is schematically depicted in Fig. 2. A plane wave with electric field amplitude E_0 and polarization $\widehat{\mathbf{e}}_{co}$ is normally incident on a device that is located near to the upper surface of a ground plane. A measure of the cross-polar component $\widehat{\mathbf{e}}_{cr}$ of the field backscattered by this combination is desired because, as noted, specular cross-polarized backscatterers are particularly relevant for data-encoding, communication and sensing applications in which an electrically small device is integrated on a large metallic object.

The projection factor for this particular scatterer-ground plane configuration reduces to

$$P_B = (\lambda^2/\pi) [E_0^2/2\eta_0] D_{\text{scat}}\left(\widehat{\mathbf{k}}_R, \widehat{\mathbf{e}}_{co}\right) \quad (8)$$

It is then convenient to describe the performance of this backscattering system by using the bistatic cross-section, which corresponds to the power scattered into a given direction / polarization pair, normalized to the incident intensity and wavelength squared, i.e.,
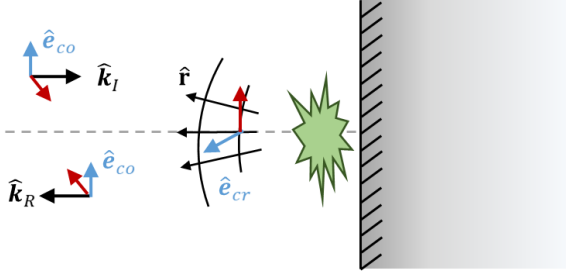
Fig. 2. Sketch of a specular cross-polarized backscatterer. A device that is located near to the top surface of a ground plane is illuminated by a normally incident plane-wave whose polarization vector is $\widehat{\mathbf{e}}_{co}$. The combination of the device and ground plane scatters the incident field into multiple directions and polarizations. The signal of interest is the cross-polarized specularly reflected field whose direction is $\widehat{\mathbf{r}} = \widehat{\mathbf{k}}_R$ and whose polarization vector is $\widehat{\mathbf{e}}_{cr}$.

$$\sigma_b\left(\widehat{\mathbf{r}}, q\right) = \mathcal{P}\left(\widehat{\mathbf{r}}, q\right) / (S_i \lambda^2) \qquad (9)$$

where the incident power density $S_i = E_0^2/(2\eta_0)$. By using these definitions in the bounds derived in the previous section, the cross-polarized version of this cross section has the upper bound:

$$\sigma_b\left(\widehat{\mathbf{k}}_R, \widehat{\mathbf{e}}_{cr}\right) \leq \frac{1}{\pi} D_{\text{scat}}\left(\widehat{\mathbf{k}}_R, \widehat{\mathbf{e}}_{cr}\right) D_{\text{scat}}\left(\widehat{\mathbf{k}}_R, \widehat{\mathbf{e}}_{co}\right) \qquad (10)$$

where $\widehat{\mathbf{e}}_{co}$ and $\widehat{\mathbf{e}}_{cr}$ label the co-pol and cross-pol unit vector directions.

In view of the bound (10), the problem of maximizing the backscattering cross-section directly aligns with simultaneously maximizing the co- and cross-polarization directivities in the reflected direction. Again, the underlying idea is that for the scattering process to be efficient, all of the scatterer must be vested in extracting as much energy from the incident field as possible and reflecting it with the desired polarization and direction. We note that both the co- and cross-polarized directivities play the same role in Eq. (10), and that they are orthogonally radiating channels. Therefore, there is no advantage to emphasizing either the scattering into the co- or cross-polar polarizations to determine the upper bound on the cross section. In fact, we can consider both directivities to be identical to obtain it. Consequently, the scattered power is taken to be equally distributed into both the co- and cross-polarization radiating channels. This also means that the corresponding directivities are identical to half the total directivity, $\mathcal{D}_{\text{scat}}$, into a single polarization state produced by the scatterer integrated with the ground plane, i.e.,

$$D_{\text{scat}}\left(\widehat{\mathbf{k}}_R, \widehat{\mathbf{e}}_{cr}\right) = D_{\text{scat}}\left(\widehat{\mathbf{k}}_R, \widehat{\mathbf{e}}_{co}\right) = \frac{1}{2}\mathcal{D}_{\text{scat}}\left(\widehat{\mathbf{k}}_R\right) \qquad (11)$$

In this manner, the upper bound (10) reduces to

$$\sigma_b\left(\widehat{\mathbf{k}}_R, \widehat{\mathbf{e}}_{cr}\right) \leq \frac{1}{4\pi}\mathcal{D}_{\text{scat}}^2\left(\widehat{\mathbf{k}}_R\right) \qquad (12)$$

The upper bound (12) reaffirms that highly directive systems are essential to achieve a large cross-polarized backscattering cross-section. Consequently, we revisit popular strategies in antenna theory to obtain a high directivity, and how they can be applied to improve the cross-polarized backscattering cross-section.

A. Electric vs Magnetic Dipoles

In order to get a deeper insight into the upper bounds for the cross-polarized backscattering cross-section of different antenna systems / scatterers placed on top of a ground plane, we start with the analysis of the most elementary scatterers, i.e., those composed of single infinitesimal electric or magnetic dipoles, also known as Hertzian dipoles. These simple examples are very relevant for the practical design of electrically small systems, and they will allow us to discuss some basic aspects of fundamental electromagnetic field-matter interactions.

For example, if an antenna element must be placed parallel and very near to a ground plane, one would be tempted to conclude that the best option would always be to use a magnetic dipole antenna because it realizes a maximum of its magnetic field there whereas an electric dipole experiences a minimum of its electric field. This intuition aligns with the concept that electromagnetic field-matter interactions are maximized by strong coupling to local fields. However, the scattering analysis indicated that electromagnetic field-matter interactions also arise as the result of interference phenomena rather than just this local field picture. In particular, the optical theorem tells us that interference phenomena are essential to the extraction of energy from the incident field and to its redirection to where it is desired. Our upper bounds of the scattering performance align with this perspective. From this point of view, we show that an electric dipole antenna in front of a ground plane would actually be preferred since it produces a higher directivity. We will demonstrate that both aspects: local interactions and interference phenomena, must be considered in a practical system to determine the best element for it to obtain an optimal performance.

To this end, we investigate the directivities that can be obtained from electric Hertzian dipole (EHD) and magnetic Hertzian dipole (MHD) antennas near to a ground plane. These configurations are shown in Fig. 3(a). First, it is straightforward to show that the end-fire directivity, $\widehat{\mathbf{r}} = \widehat{\mathbf{x}}$, of an EHD with its current moment parallel to the ground plane at a distance d from it is given by

$$D_{\text{EHD}}\left(\widehat{\mathbf{x}}\right) = 2\frac{1 - \cos\gamma}{\frac{2}{3} - \frac{\sin\gamma}{\gamma}\left(1 - \frac{1}{\gamma^2}\right) - \frac{\cos(\gamma)}{\gamma^2}} \qquad (13)$$

where $\gamma = 2kd$. It is interesting to point out some relevant limits: (i) $D_{\text{EHD}} \to 0$ when $\gamma \to n\pi$. This end-fire direction outcome corresponds to the destructive interference between the EHD and its image in the ground plane. (ii) $D_{\text{EHD}} \to 4/[\frac{2}{3} + \frac{1}{(2n+1)^2\pi^2}] \simeq 6$ when $\gamma \to (n + 1/2)\pi$. This end-fire direction outcome corresponds to constructive interference between the EHD and its image in the ground plane. (iii)
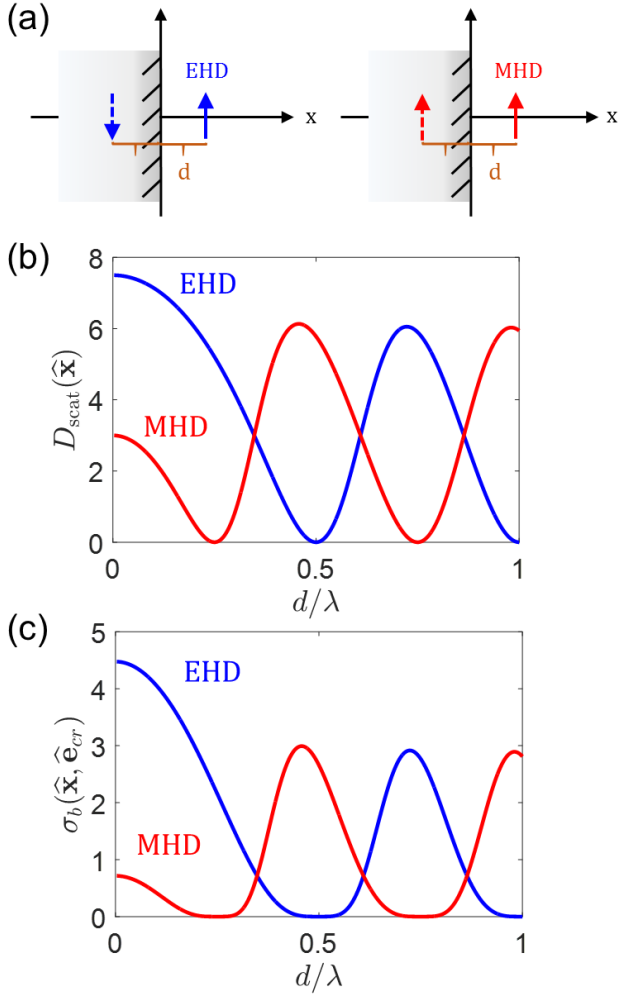
Fig. 3. (a) Sketch of elementary electric Hertzian dipole (EHD) and magnetic Hertizan dipole (MHD) sources whose current moments are oriented parallel to the ground plane at a distance of separation d from it. (b) Directivity of the EHD and MHD sources as a function of the separation distance to the ground plane. (c) Upper bound of the cross-polarized backscattering cross-section for antenna systems whose scattering response can be approximated by that of these elementary EHD and MHD sources.

$D_{\text{EHD}} \to 7.5$ in the $\gamma \to 0$ limit. This maximum directivity for an EHD surprisingly occurs when the separation with respect to the ground plane vanishes. This directivity enhancement in the $\gamma \to 0$ limit is the result of strong destructive interference and is analogous to what occurs with superdirective antenna configurations. In particular, the fields excited by the image in the ground plane tend to cancel those of an EHD as it is brought close to the ground plane. However, this destructive interference effect is weighted differently for different observation directions. Those fields radiated in directions with a larger phase difference are penalized less, i.e., in the end-fire direction corresponding to the axis joining the dipole and its image. This interference phenomenon gives rise to a highly directive pattern.

On the other hand, the end-fire directivity of a MHD under the same conditions is given by

$$D_{\text{MHD}}(\widehat{\mathbf{x}}) = 2 \frac{1 + \cos(\gamma)}{\frac{2}{3} + \frac{\sin\gamma}{\gamma}\left(1 - \frac{1}{\gamma^2}\right) + \frac{\cos\gamma}{\gamma^2}} \tag{14}$$

The associated limits are then: (i) $D_{\text{MHD}} \to 4/[\frac{2}{3} + \frac{1}{(2n+1)^2\pi^2}] \simeq 6$ when $\gamma \to n\pi$. (ii) $D_{\text{MHD}} \to 0$ when $\gamma \to (n+1/2)\pi$, again corresponding to the constructive and destructive interference conditions in the end-fire direction. (iii) $D_{\text{MHD}} \to 3$ in the limit $\gamma \to 0$, showing the well known factor of 2 directivity enhancement for a MHD as its separation with the ground plane vanishes.

The directivity for antenna systems whose response can be approximated by that of EHDs and MHDs in front of a ground plane is presented in Fig. 3(b). The associated upper-bound on the cross-polarized backscattering cross section that could be obtained with pairs of two orthogonal EHDs or MHDs is reported in Fig. 3(c). As anticipated, an EHD produces a higher directivity than a MHD as $d \to 0$, leading to an upper bound on the cross-polarized backscattering cross-section that is 6.25 times higher. This result indicates that EHDs can in theory provide a superior backscattering performance than MHDs in the proximity of a ground plane. Their higher directivity makes them an efficient element that extracts the most energy from the incident field during the scattering process.

However, similar to superdirective systems, the directivity enhancement of a EHD next to a ground plane is obtained by means of a general destructive interference that can negatively affect the backscattering performance in the presence of losses, i.e., when dissipation damping is comparable to or greater than radiation damping. We further investigate this effect and its practical implementation by designing a small cross-polarized scatterer whose response can be approximated by that of two orthogonal EHDs. As depicted in Fig. 4(a), it consists of a copper strip printed on the top surface of a Rogers Duroid^{TM} copper-cladded substrate with its bottom surface being the ground plane. Its asymmetric geometry has been designed to maximize the cross-polarized scattering cross-section. Its details are reported in Fig. 4(b). The entire structure is contained within a radius of 15 mm (0.105λ at 2.1 GHz). The fields scattered by this element are similar to those of two orthogonal EHDs except for the fact that the maximum directivity of each dipole is slightly larger, 1.68 instead of 1.5, due to its nonzero physical size.

Fig. 4(c) shows the cross-polarized backscattering cross-section as a function of frequency for several separation distances to the ground plane. The backscattering cross-section is characterized by a resonant peak near 2.1 GHz that slightly shifts towards lower frequencies as the separation distance decreases. In addition, the resonance linewidth decreases along with the separation distance, which can be understood as the results of a smaller radiation damping. A closer connection between the performance of the system and our theory can be found by inspecting the peak backscattering cross-section as a function of d, as well as its comparison with the lossless implementations of the system and the theoretical upper bound (shown in Fig. 4(d)). In the lossless case, our design reaches the theoretical upper bound and its backscattering cross-
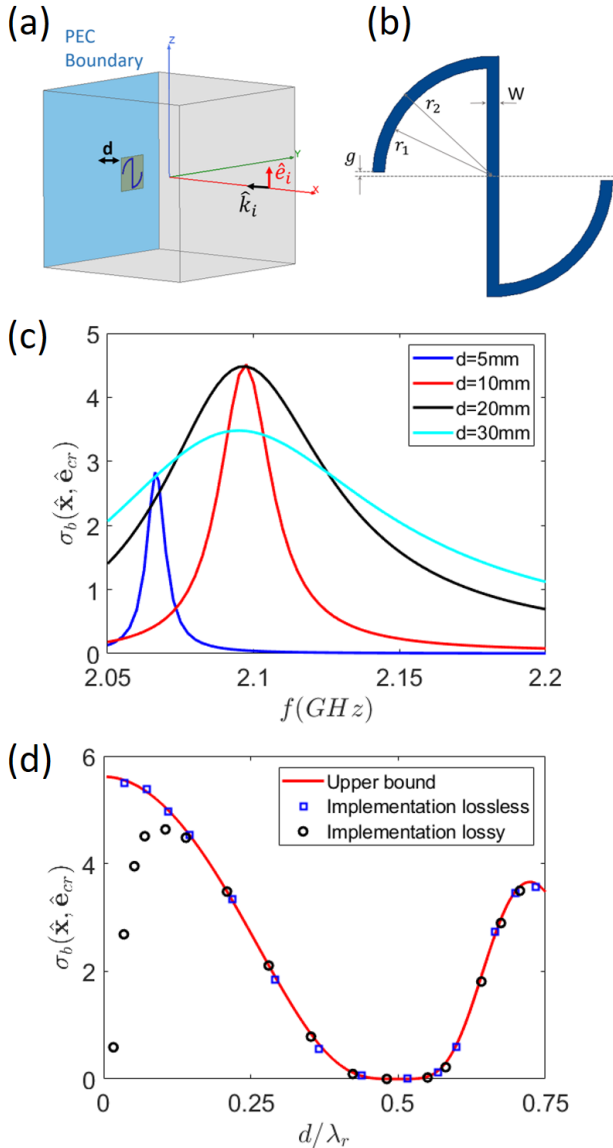
Fig. 4. (a) The ANSYS high frequency structure simulator (HFSS) model of an asymmetric, cross-polarized backscatterer located at a distance d from a ground plane and printed on the surface of a dielectric. It is excited by a plane wave with its electric field polarized parallel to the dipole axis. (b) Top-view and additional details of the element's geometry. Relevant design parameter values in millimeters (mm) are: $W = 1.5$, $r_2 = 15$, $r_1 = 13.5$ and $g = 0.5$. The scattering element is printed as $70\,\mu m$ thick copper traces on the top surface of a 0.254 mm thick Rogers RO5880 substrate whose dielectric constant is 2.2 and loss tangent is 0.0009. (c) Cross-polarized backscattering cross-section as a function of frequency for different separations to the ground plane. (d) Comparison of the cross-polarized backscattering cross-section predicted for the asymmetric dipole in its lossless and lossy implementations and the theoretical upper bound of the cross-polarized backscattering cross-section, scaled to account for its maximum free-space scattering directivity, 1.68, associated with its nonzero geometrical size. The wavelength at the resonance frequency λ_r is defined as the wavelength at the resonance peaks.

section can be considered optimal. This result suggests that carefully engineering the interference phenomena is indeed the dominant feature needed to optimize the backscattering cross-section. However, once losses are introduced in the design, the backscattering cross-section approaches zero as the separation distance does. This effect is a result of the fact that

the radiation resistance becomes asymptotically zero for an EHD on top of a ground plane. Nevertheless, we note that the maximal cross-polarized backscattering cross-section for the theoretical MHD configuration is only 0.7162, and the lossy EHD reaches that value for a separation distances around $d = 0.015\lambda$. Therefore, these numerical simulations show that lossy electric dipole antennas, with their enhanced directivity, actually provide a higher backscattering even for relatively small separation distances.

On the other hand, our results suggest that MHD elements should be selected for extremely low profiles, provided that a planar MHD design is available. In order to shed more light into this point, we have designed and numerically simulated a small cross-polarized backscatterer whose response can be approximated by that of two crossed MHDs. The backscatterer consists of a copper capacitively loaded loop printed on the top surface of a Rogers Duroid^{TM} copper-cladded substrate, as shown in Figs. 5(a) and 5(b). Similar to the practical implementation for the EHD case, the entire structure of the backscatterer is contained within a radius of 15 mm. The fields scattered by this element are similar to those of two crossed MHDs except for the fact that the maximum directivity of each dipole is 1.90 instead of 1.5, due to its geometry and nonzero geometrical size. The desired cross-polarized backscattering performance is obtained by means of a $45°$ rotation of the loop with respect to the direction of the incident electric field.

As schematically depicted in the top panel of Fig. 5(a), the geometry of a realistic loop with a magnetic dipole moment parallel to the ground plane occupies a certain area that limits how close to the ground plane the center of the scatterer can be. However, an equivalent performance to that obtained for the zero distance $d = 0$ case can be achieved by cutting this structure in half. The resulting structure, schematically depicted in the bottom panel of Fig. 5 (a), relies on the fact that the image in the ground plane reproduces the original geometry.

Fig. 5(d) shows the numerically simulated cross-polarized backscattering cross-section and the theoretical upper bound in both the lossless and lossy implementations of the magnetic resonator in front of a ground plane. An excellent agreement is observed between the theoretical and numerically simulated results, demonstrating that the proposed theory can be applied to scatterers whose response can be approximated by that of crossed MHDs. As expected, the magnetic resonator is less affected by losses than its electric counterpart for small separation distances. Similarly, no dramatic decrease of the bandwidth is observed for small separation distances, as shown in Fig. 5(c).

However, this numerical example reaffirms the theoretical conclusion that the backscattering from a MHD in the presence of a ground plane is smaller than its electric counterpart. In addition, analyzing a realistic implementation highlights that designs inspired by the MHD configuration might in practice require a higher profile. For example, due to the nonplanar shape of the MHD, the total profile for the $d = 0$ case is actually comparable to the EHD case with $d = 15\,\mathrm{mm}$. To sum up, our theory and numerical simulations show that lossy electric dipole antennas, with their enhanced directivity,
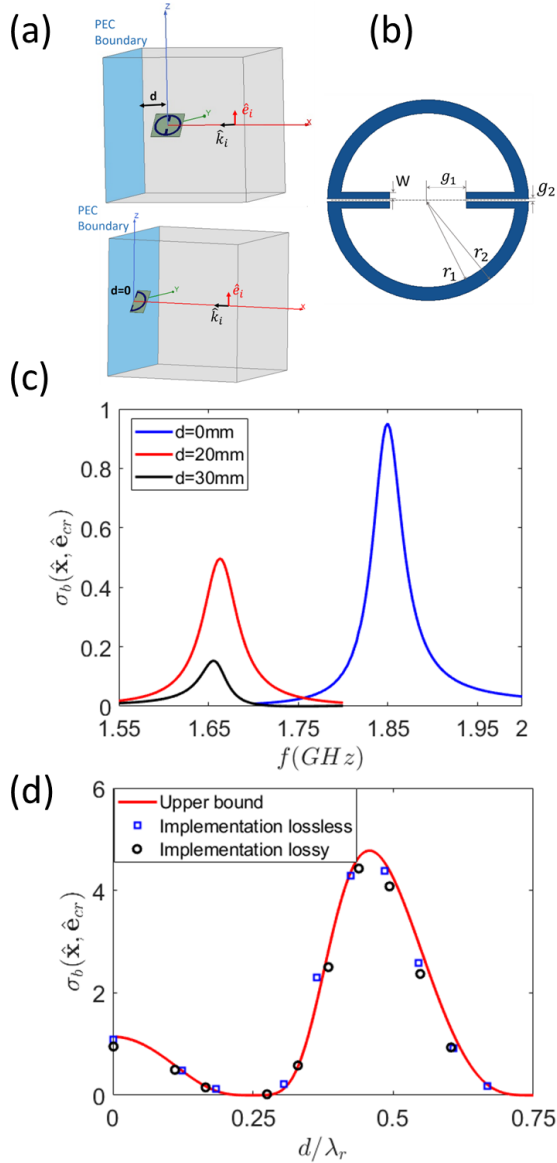
Fig. 5. A magnetic resonator located at a distance d from a ground plane and printed on the surface of a dielectric sheet. It is excited a plane wave whose electric field is polarized at 45 degrees with respect to the plane of the resonator in order to obtain a cross-polarized performance. (a) ANSYS high frequency structure simulator (HFSS) model. (b) Top-view and additional details of the element's geometry. Relevant design parameters in millimeters (mm) are: $W = 1$, $r_1 = 13$, $r_2 = 15$, $g_1 = 5.7$ and $g_2 = 0.4$. The scattering element is printed as $70\,\mu m$ thick copper traces on the top surface of a 0.254 mm thick Rogers RO5880 substrate whose dielectric constant is 2.2 and loss tangent is 0.0009. (c) Cross-polarized backscattering cross-section as a function of frequency for different distances from the ground plane. (d) Comparison of the cross-polarized backscattering cross-section predicted for the magnetic resonator in its lossless and lossy implementations and the theoretical upper bound of the cross-polarized backscattering cross-section. It has been scaled to account for its maximum free-space scattering directivity, 1.90, associated with its geometry and nonzero geometrical size. The wavelength at the resonance frequency λ_r is defined as the wavelength at the resonance peaks.

actually provide a larger backscattering response even for relatively small separation distances. Therefore, both local field interactions and interference phenomena must be taken into account in practice to determine the optimal choice of the radiating/scattering elements.

B. Huygens source antennas

Another design strategy for highly-directive electrically small antennas is that of Huygen's source antennas (HSAs) [35]–[37]. The HSAs are properly balanced combinations of orthogonal EHD and MHD radiators. They are characterized by a cardioid radiation pattern with a peak directivity of 3, being the maximal value that can be obtained without the excitation of higher-order modes. Moreover, this directivity enhancement of the HSAs is not penalized in terms of bandwidth and efficiency when compared to individual EHD and MHD radiators. For these reasons, HSAs have been investigated in a number of systems, including low-profile [38], non-Foster [39], reconfigurable [40], on-chip [41] and wireless power transfer [42] antennas.

Unfortunately, the integration of a HSA with a ground plane is not a trivial task. The main difficulty arises from the fact that EHD and MHD have images of opposing polarity in the ground plane. Consequently, their optimal combination can be very different from that in free-space. In the following, we report the directivity of HSAs integrated with a ground plane, as well as the upper bound on the cross-polarized backscattering cross-section that can be obtained with systems whose response can be approximated by a combination of Hertzian dipoles.

As schematically depicted in Fig. 6(a), we consider a HSA constructed as the combination of an EHD and a MHD placed at a distance d from a ground plane whose current moments are orthogonal and parallel to it. Performing the necessary integrations to obtain the far-field power, it is found that the directivity of the HSA-ground plane combination can be explicitly written as:

$$D_{\mathrm{HSA}}\left(\widehat{\mathbf{x}}\right) =$$
$$4\,\frac{\left|a_1\right|^2 \sin^2\left(\frac{\gamma}{2}\right) + \left|a_2\right|^2 \cos^2\left(\frac{\gamma}{2}\right) + \frac{\beta(a_1,a_2)}{2}\sin\left(\gamma\right)}{\left|a_1\right|^2 \alpha_1(\gamma) + \left|a_2\right|^2 \alpha_2(\gamma) + \beta(a_1,a_2)\left(\frac{\sin\gamma}{\gamma^2} - \frac{\cos\gamma}{\gamma}\right)} \tag{15}$$

where a_1 and a_2 are the excitations coefficients of the EHD and MHD, respectively, and the following definitions have been introduced:

$$\beta\left(a_1,a_2\right) = a_1 a_2^* + a_2 a_1^* \tag{16}$$

$$\alpha_1\left(\gamma\right) = \frac{2}{3} - \frac{\sin\gamma}{\gamma}\left(1 - \frac{1}{\gamma^2}\right) - \frac{\cos\gamma}{\gamma^2} \tag{17}$$

$$\alpha_2\left(\gamma\right) = \frac{2}{3} + \frac{\sin\gamma}{\gamma}\left(1 - \frac{1}{\gamma^2}\right) + \frac{\cos\gamma}{\gamma^2} \tag{18}$$

For a conventional HSA with balanced EHD and MHD elements, i.e., with $a_1 = a_2$, the directivity (15) reduces to

$$D_{\mathrm{HSA}}\left(\widehat{\mathbf{x}}\right)\big|_{a_1=a_2} = 2\,\frac{1 + \sin\gamma}{\frac{2}{3} + \frac{\sin\gamma}{\gamma^2} - \frac{\cos\gamma}{\gamma}} \tag{19}$$

This directivity and the associated upper bound on the cross-polarized backscattering cross-section are depicted in Figs. 6(b) and 6(c), respectively, as functions of the separation distance d. For large separation distances giving $\gamma \gg 1$, the directivity of the conventional HSA reduces to $3\left(1 + \sin\gamma\right)$,
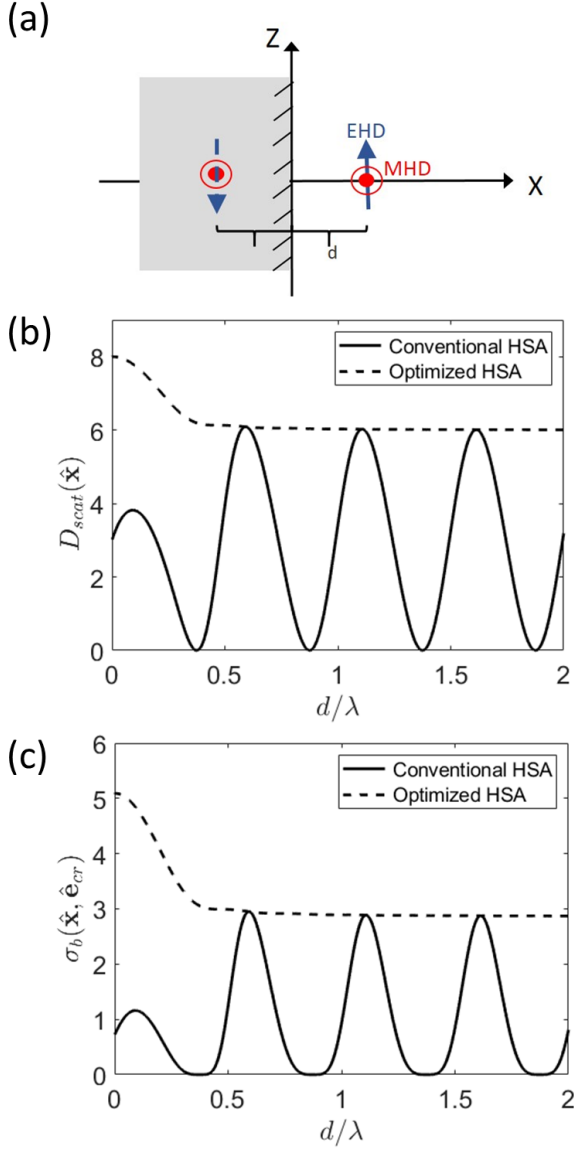
Fig. 6. (a) Sketch of a Huygens source antenna (HSA), consisting of a pair of orthogonal electric Hertzian dipole (EHD) and magnetic Hertizan dipole (MHD) elementary sources placed at a distance d from the ground plane with their current moments oriented parallel to it. (b) Directivity of the conventional HSA, with balanced electric and magnetic dipoles, $a_1 = a_2$, and the optimized HSA as functions of the separation to the ground plane distance d. The optimal coefficients were found by solving a generalized eigenvalue problem (20). (c) Upper bound of the cross-polarized backscattering cross-section for antenna systems whose scattering response can be approximated by that of both elementary electric and magnetic dipole sources.

i.e., it exhibits a simple sinusoidal behavior. On the other hand, for small separation distances where $\gamma \to 0$, it converges to 3, i.e., the same value as that of the directivity of a MHD near the ground plane. This result stems from the fact that the power radiated by an EHD vanishes near the ground plane. Therefore, the response of the system for fixed current moments asymptotically approaches that of the MHD. These results show that the conventional HSA does not provide any directivity enhancement when it is placed in close proximity to a ground plane. They also indicate that a substantially larger electric current moment would be needed in order to observe

consequential interference effects arising from the interplay between the electric and magnetic dipoles of a HSA placed near a ground plane.

For these reasons, we focus on finding the optimal complex coefficients, a_1 and a_2, that maximize the directivity of the system. To this end, we rewrite Eq. (15) in the form of a generalized Rayleigh quotient, whose maximization can be cast as a generalized eigenvalue problem [43], [44]:

$$D\left(\widehat{\mathbf{x}}\right) = \frac{\mathbf{a}^{\dagger} \cdot \mathbf{F}\left(\widehat{\mathbf{x}}\right) \cdot \mathbf{a}}{\mathbf{a}^{\dagger} \cdot \mathbf{H} \cdot \mathbf{a}} \tag{20}$$

where $\mathbf{a} = [a_1, a_2]^T$ is the excitation vector. The terms $\mathbf{F}$ and $\mathbf{H}$ are 2×2 (symmetric and positive semidefinite) matrices defined as:

$$\mathbf{F}\left(\widehat{\mathbf{x}}\right) = 4 \begin{bmatrix} \sin^2\left(\frac{\gamma}{2}\right) & \sin\left(\frac{\gamma}{2}\right)\cos\left(\frac{\gamma}{2}\right) \\ \sin\left(\frac{\gamma}{2}\right)\cos\left(\frac{\gamma}{2}\right) & \cos^2\left(\frac{\gamma}{2}\right) \end{bmatrix} \tag{21}$$

$$\mathbf{H} = \begin{bmatrix} \alpha_1\left(\gamma\right) & \frac{\sin\gamma}{\gamma^2} - \frac{\cos\gamma}{\gamma} \\ \frac{\sin\gamma}{\gamma^2} - \frac{\cos\gamma}{\gamma} & \alpha_2\left(\gamma\right) \end{bmatrix} \tag{22}$$

The directivity resulting from this optimization process, as well as the associated upper bound on the cross-polarized backscattering cross-section, as functions of the separation distance d are reported in Figs. 6(b) and 6(c), respectively. For large separation distances, $\gamma \gg 1$, the directivity converges to the constant value 6. This behavior can be explained as follows.

First note that in the limit $\gamma \to \infty$ the directivity (15) becomes

$$\lim_{\gamma \to \infty} D_{\mathrm{HSA}}\left(\widehat{\mathbf{x}}\right) = 6 \frac{\left|a_1 \sin\left(\frac{\gamma}{2}\right) + a_2 \cos\left(\frac{\gamma}{2}\right)\right|^2}{\left|a_1\right|^2 + \left|a_2\right|^2} \tag{23}$$

Equation (23) shows that the cross-terms only contribute to the numerator, i.e., the total power radiated by the EHD and MHD decouples, similar to the free-space case. Therefore, the directivity is simply maximized when the fields radiated in the end-fire direction add in phase. In particular, it can be found from Eq. (23) that the optimal coefficients are given by $a_1 = \sin(\gamma/2)$ and $a_2 = \cos(\gamma/2)$. Therefore, the optimal value for the directivity is $D_{\mathrm{HSA}}\left(\widehat{\mathbf{x}}\right) = 6$ for large separation distances. This outcome equals that of the peaks of the EHD and MHD directivities in the same regime. Nevertheless, the proper combination of EHD and MHD makes it possible to obtain that same value for any separation distance in the $\gamma \gg 1$ regime.

For small separation distances where $\gamma \to 0$, Fig. 6(b) shows that the directivity converges to an optimal value of 8, which is only slightly larger than the 7.5 that was obtained for the EHD alone. Additional insight on this value can be obtained by noting that in the $\gamma \to 0$ limit Eq. (15) reduces to

$$\lim_{\gamma \to 0} D_{\mathrm{HSA}}\left(\widehat{\mathbf{x}}\right) = 4 \frac{\left|a_1\right|^2 \left(\frac{\gamma}{2}\right)^2 + \left|a_2\right|^2 + \beta(a_1, a_2)\frac{\gamma}{2}}{\frac{2}{15}\left|a_1\right|^2 \left(\gamma\right)^2 + \frac{4}{3}\left|a_2\right|^2 + \frac{1}{3}\beta(\gamma)} \tag{24}$$

From Eq. (24) it can be found that the optimal coefficients in the $\gamma \to 0$ limit are given by $a_1 = -10a_2/\gamma$.

This solution confirms that the electric current moment has to be increased as the separation distance decreases in order to observe interference phenomena between the fields radiated by the EHD and MHD sources. In addition, it clearly shows that the optimal configuration is very different from that of the conventional free-space HSAs. In fact, the combination of EHD and MHD with $a_1 = -10a_2/\gamma$ coefficients in free-space maximizes the radiation in the direction $\widehat{\mathbf{r}} = \widehat{\mathbf{x}}$. Moreover, these optimal coefficients lead to a maximal directivity $D_{\text{HSA}}(\widehat{\mathbf{x}}) = 8$ that is only slightly higher than that of an EHD $D_{\text{EHD}}(\widehat{\mathbf{x}}) = 7.5$. Therefore, our analysis concludes that an optimized, balanced combination of an electric and magnetic dipole in the proximity of a ground plane does not provide a significant enhancement of the directivity of the end-fire radiation as it does in free-space. Consequently, this strategy in the design of cross-polarized tags has limited applicability, particularly considering the complexity involved in the design of an optimized HSA that must operate with both polarizations to generate a cross-polarized backscattering signal.

C. End-fire arrays

Superdirective end-fire arrays are one of the classic approaches to achieve an enhanced directivity. Starting with the early work by Uzkov [45], which demonstrated that the directivity of an end-fire array of N isotropic radiators converges to N^2 as the separation between the elements tends to zero, the radiation [46] and scattering [25] performance of end-fire arrays has been actively investigated. In fact, it has been demonstrated that electrically small end-fire arrays provide the highest achievable directivity for any 3D configuration with a fixed number of radiators [47]. Admittedly, the practical implementation of superdirective arrays is hindered by their sensitivity to dissipation losses and fabrication tolerances. Nonetheless, there have been a number of successful experimental demonstrations of electrically small end-fire antenna arrays [48]–[53]. We have analyzed their performance when integrated with a ground plane and have obtained the corresponding upper bound of the cross-polarized backscattering cross-sections.

1) End-fire array of EHDs: Fig. 7(a) depicts the geometry of an end-fire array of N electric Hertzian dipoles whose current moments are parallel to the Z-axis, $\mathbf{Idl}_n = \widehat{\mathbf{z}}\, a_n I_0 dl$, and are separated by the constant separation distance, $2d$, along the X-axis. The first element is placed at a distance d from the ground plane, i.e., $\mathbf{r}_n = \widehat{\mathbf{x}}\,(2n-1)\,d$ with $n = 1, \ldots, N$. The directivity of this end-fire array can again be written as a generalized Rayleigh quotient following Eq. (20), where $\mathbf{a} = [a_1, \ldots, a_n]^T$ is now the excitation vector and the elements of the $\mathbf{F}(\widehat{\mathbf{r}})$ and $\mathbf{H}$ matrices are given by

$$F_{mn}(\widehat{\mathbf{r}}) = 2\sin^2\theta \sin(c_n \sin\theta\cos\phi)\sin(c_m\sin\theta\cos\phi) \tag{25}$$

$$H_{mn} = \frac{1}{2\left(c_{mn}^-\right)^3}\left[\left(\left(c_{mn}^-\right)^2 - 1\right)\sin c_{mn}^- + c_{mn}^-\cos c_{mn}^-\right]$$
$$- \frac{1}{2\left(c_{mn}^+\right)^3}\left[\left(\left(c_{mn}^+\right)^2 - 1\right)\sin c_{mn}^+ + c_{mn}^+\cos c_{mn}^+\right] \tag{26}$$
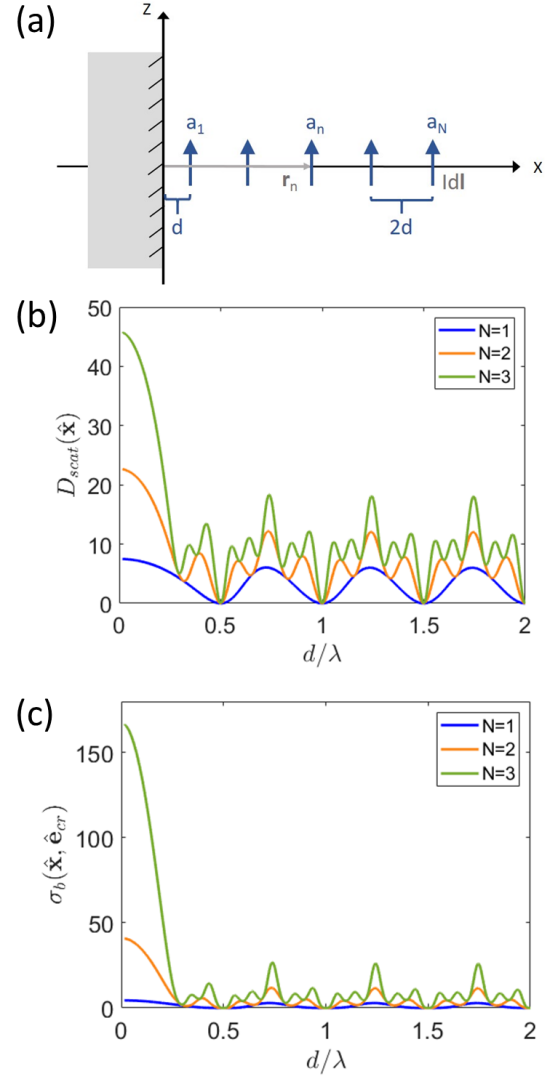

Fig. 7. (a) Sketch of an end-fire array of N EHD dipoles separated by a constant distance $2d$ with the first element placed at a distance d from the ground plane. (b) Maximum directivity of this configuration in the end-fire direction. (c) Upper-bound of the cross-polarized backscattering cross-section as a function of the separation distance for arrays of $N = 1$, 2 and 3 elements. It was obtained by numerically solving the associated generalized eigenvalue problem.

where the terms $c_n = \left(n - \frac{1}{2}\right)\gamma$ and the off-diagonal coefficients $c_{mn}^\pm = |c_m \pm c_n|$. The diagonal elements with $n = m$ are

$$H_{nn} = \frac{1}{3} - \frac{1}{2\left(c_{nn}^+\right)^3}\left[\left(\left(c_{nn}^+\right)^2 - 1\right)\sin c_{nn}^+ + c_{nn}^+\cos c_{nn}^+\right] \tag{27}$$

Figs. 7(b) and 7(c) show the maximal directivity obtained in the end-fire direction, $\widehat{\mathbf{r}} = \widehat{\mathbf{x}}$, and the upper-bound of the cross-polarized backscattering cross-section, respectively. The latter was computed by numerically solving the associated generalized eigenvalue problem. Both figures of merit are depicted as functions of the separation distance d for arrays of $N = 1$, $N = 2$ and $N = 3$ elements. At large separation distances, the directivity is again characterized by

an oscillatory behavior with peak values equal to $6N$ at the points where constructive interference in the end-fire direction occurs. Even higher values are obtained in the small separation limit with directivities of 7.5, 22.70 and 45.88 for the arrays with $N = 1$, 2 and 3 elements. Consequently, arrays of 2 and 3 elements result in enhancement factors of 9.18 and 37.45 for the cross-polarized backscattering cross-section. In conclusion, the cross-polarized backscattering cross-section can be significantly enhanced even by using arrays with a small number of elements.

In view of these positive theoretical results, there is a clear motivation to numerically verify how this enhancement can be obtained and to determine what the impact of loss is on its practical implementation. However, the design of electrically small superdirective arrays is not without challenges. First, we note that the theoretical upper bound is obtained by means of an optimization procedure that identifies the optimal excitation coefficients for the dipoles. Therefore, each point of the theoretical curve in Fig. 7 implies carrying out a dedicated design providing the proper combination of excitation coefficients, including the task of managing the influence of the ground plane and the coupling between the dipoles. As an illustrative example, we have numerically simulated an array of two identical electric dipoles, using the same element geometry as in the EHD case, Fig. 4. This dipole end-fire array configuration is shown in Figs. 8(a) and 8(b). The simulation results are included in Fig. 8(c). The obtained values of the cross-polarized backscattering cross-section are close, but slightly below the upper bound. As anticipated, matching the upper bound requires a dedicated design for each separation distance, particularly within the superdirective regime.

At the same time, our particular design closely approaches the optimal configuration near $d = 0.2\lambda$, where the predicted value for our design is 24.22. This peak value is 4.36 times larger than the optimal value predicted for a single element in the $d \to 0$ limit in Fig. 4. In addition, this value represents a 1.63 times enhancement with respect to the theoretical upper bound for the local maxima at larger separation distances that correspond to the conventional array configurations based on constructive interference. In this manner, this example serves to validate that superdirective arrays enable an enhanced backscattering cross-section with a reduced profile. In addition, the numerical simulations reveal that losses do not have an acute detrimental effect for this particular design. However, it is expected that superdirective designs with an even smaller separation distance will be more strongly affected by dissipation losses.

2) End-fire array of MHD: Although end-fire arrays of EHDs provide high directivities in the small distance of separation limit, the fact that the radiation from all of the elements tends to zero hinders their practical implementation if a deeply subwavelength profile is required. On the other hand, an array of MHDs would be a preferred alternative for such a very low-profile configuration as an extrapolation from the end-fire array of EHDs treated above. The possibility that this configuration would indeed provide a high directivity is considered with the end-fire array of MHDs having the same
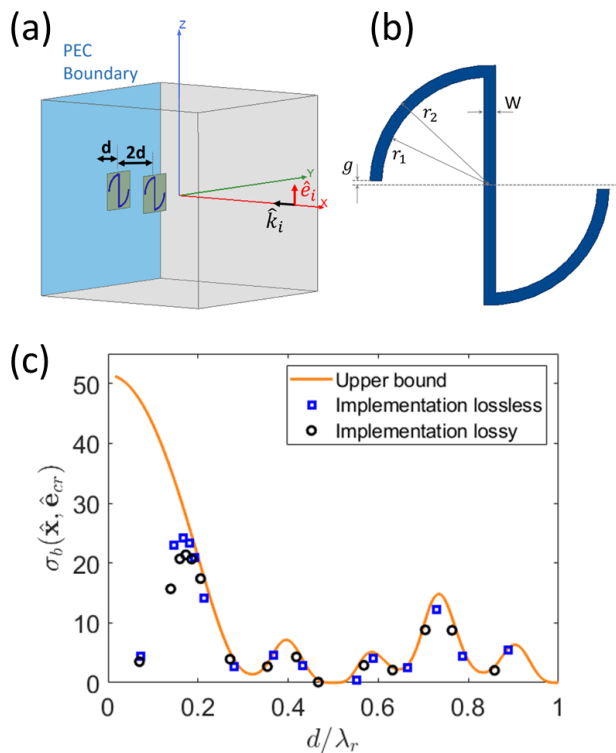

Fig. 8. Simulated performance of a two-element end-fire array of EHDs located at a distance d from a ground plane with a separation distance $2d$ between both dipoles. The elements in the array are asymmetric cross-polarized backscatterers printed on the surface of a dielectric sheet. The array is excited by a plane wave with its electric field polarized parallel to the axes of the dipoles. (a) ANSYS high frequency structure simulator (HFSS) model. (b) Top-view and additional details of the element's geometry. Relevant design parameters in millimeters (mm) are: $W = 1.5$, $r_1 = 13.5$, $r_2 = 15$ and $g = 0.4$. The scattering element is printed as $70\,\mu$m thick copper traces on the top surface of a 0.254 mm thick Rogers RO5880 substrate whose dielectric constant is 2.2 and loss tangent is 0.0009. (c) Cross-polarized backscattering cross-section as a function of frequency for different separations to the ground plane. (d) Comparison of the cross-polarized backscattering cross-section predicted for the end-fire array in its lossless and lossy implementations and the theoretical upper bound of the cross-polarized backscattering cross-section, scaled to account for the maximum free-space scattering directivity of the dipoles. The wavelength at the resonance frequency λ_r is defined as the wavelength at the resonance peaks.

configuration studied as the EHDs in Fig. 9(a). The associated $\mathbf{F}\left(\hat{\mathbf{r}}\right)$ and $\mathbf{H}$ matrix elements are:

$$F_{mn} = 2\sin^2\theta\cos\left(c_n\sin\theta\cos\phi\right)\cos\left(c_m\sin\theta\cos\phi\right) \quad (28)$$

$$H_{mn} = \frac{1}{2\left(c_{mn}^-\right)^3}\left[\left(\left(c_{mn}^-\right)^2 - 1\right)\sin c_{mn}^- + c_{mn}^-\cos c_{mn}^-\right]$$
$$+ \frac{1}{2\left(c_{mn}^+\right)^3}\left[\left(\left(c_{mn}^+\right)^2 - 1\right)\sin c_{mn}^+ + c_{mn}^+\cos c_{mn}^+\right] \quad (29)$$

$$H_{nn} = \frac{1}{3} + \frac{1}{2\left(c_{nn}^+\right)^3}\left[\left(\left(c_{nn}^+\right)^2 - 1\right)\sin c_{nn}^+ + c_{nn}^+\cos c_{nn}^+\right]$$
$$(30)$$

Figs. 9(b) and 9(c) show the obtained maximal directivity in the end-fire direction ($\hat{\mathbf{r}} = \hat{\mathbf{x}}$) and the upper bound for the cross-polarized backscattering cross-section. Again, they are computed by numerically solving the associated generalized

eigenvalue problem. The results are depicted as functions of the separation distance d for arrays of $N = 1$, $N = 2$ and $N = 3$ elements. The behavior at large separation distances is characterized by oscillations exhibiting peaks with a $6N$ value as was found for the EHD end-fire array.
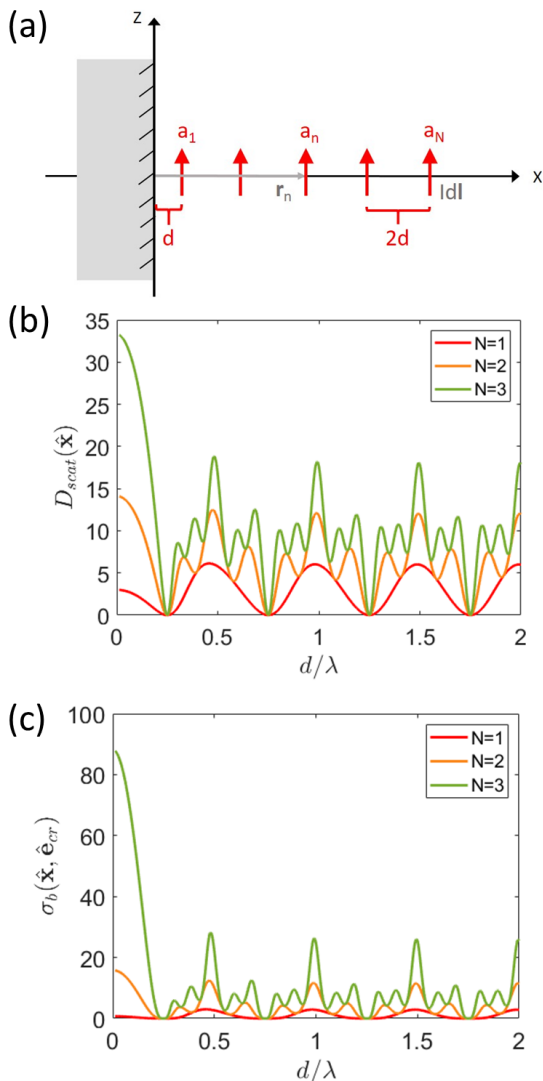
integrated on top of a ground plane provided that low-profile designs for the MHD resonators can be identified.

Fig. 9. (a) Sketch of an end-fire array of N MHD dipoles separated by a distance $2d$, with the first element placed at a distance d from the ground plane. (b) Maximum directivity in the end-fire direction and (c) upper-bound of the cross-polarized backscattering cross-section, obtained by numerically solving the associated generalized eigenvalue problem, as a function of the separation distance, and for arrays of $N = 1$, 2 and 3 elements.

It can also be concluded from these figures that the maximum directivity is observed in the vicinity of the ground plane for MHD arrays of $N = 2$ and $N = 3$ elements, unlike the behaviour for a single MHD. Specifically, the values of the directivity in the $\gamma \to 0$ limit are 3, 14.12 and 33.29 for the arrays of $N = 1$, 2 and 3 elements. This result suggests that end-fire arrays of MHDs should be considered for the practical realization of cross-polarized backscatterers. For example, the directivity of an end-fire array of 2 MHDs is larger than that of a single EHD. Thus, the array might represent a very competitive strategy for the design of cross-polarized tags
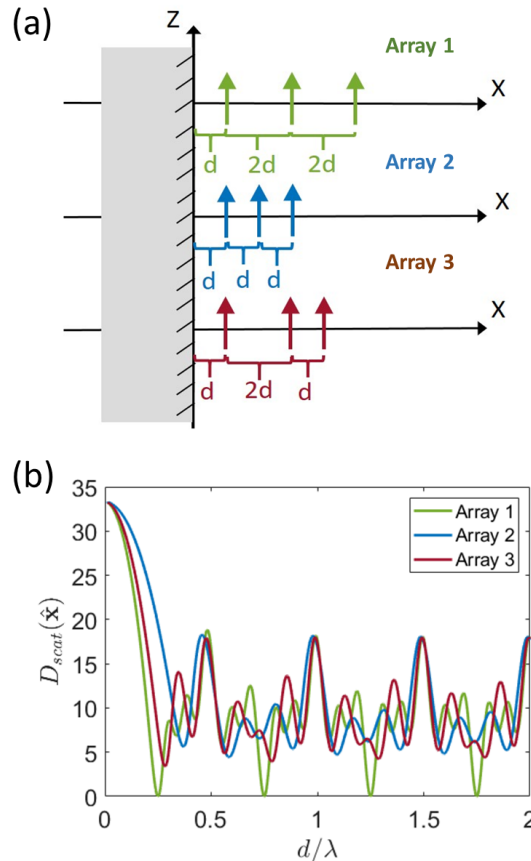

Fig. 10. (a) Sketch of three end-fire arrays of $N = 3$ MHD dipoles oriented parallel to the ground plane and positioned in different configurations with d representing the length-scale factor for the separation distance between the elements. (b) Maximum directivity in the end-fire direction as a function of the length-scale factor d obtained by numerically solving the associated generalized eigenvalue problem. The numerical results clearly demonstrate that the directivity in the $d \to 0$ limit is the same independent of the positioning configuration.

To finalize our analysis, it is noted that we have chosen a specific array geometry that preserves a constant separation distance between the entire array including the radiating elements and their images in the ground plane. Therefore, it was important to consider how this specific choice affects the reported conclusions. To shed more light on this issue, Fig. 10 depicts the directivity obtained for three different arrays of $N = 3$ MHD dipoles integrated with a ground plane that have different positioning configurations. It is concluded from the figure that changes in the position of the elements critically affects the maxima and minima of the directivity observed in the $d/\lambda \gg 1$ limit. At the same time, all of the tested configurations converge to the same value for the directivity in the $d \to 0$ limit. Therefore, it can be stated that the conclusions previously drawn for the very low-profile end-fire arrays will hold quite independently of their uniform or non-uniform configurations.

IV. CONCLUSION

It was demonstrated that highly-directive scattering systems provide a superior cross-polarization backscattering performance when their scatterers are integrated with a ground plane. An analysis based on the optical theorem indicates that the projection of the scattered field onto the reflected field is essential to enable an efficient extraction of energy from any number of scattering processes. The analysis was particularized to the case of cross-polarized specular reflection. It provides useful design guidelines for scatterers inspired by well-known basic antennas. For example, it was concluded that EHD scatterers theoretically provide larger cross-sections than their magnetic counterparts due to their higher directivity. It was shown that the use of Huygens source systems and/or optimal combinations of EHD and MHD scatterers do not provide a significant enhancement with respect to the performance of individual elementary dipoles. On the other hand, it was demonstrated that end-fire arrays can provide a significant enhancement even for two-element arrays.

The theoretical upper bounds were tested numerically with both realistic symmetric and asymmetric single elements and a two-element array of the asymmetric element in the presence of a ground plane. These cross-polarized backscattering examples reached the upper bounds, confirming their efficacy. Their lossless and lossy versions helped characterize issues in the superdirective regimes. We believe that our theoretical results and pathfinder elements will find applicability in the design of electrically small scattering systems for different sensing, storage and communication applications.

ACKNOWLEDGMENT

REFERENCES

[1] C. Herrojo, F. Paredes, J. Mata-Contreras, and F. Martín, "Chipless-RFID: a review and recent developments," *Sensors*, vol. 19, no. 15, p. 3385, Aug. 2019.

[2] F. Costa, S. Genovesi, and A. Monorchio, "Chipless RFIDs for metallic objects by using cross polarization encoding," *IEEE Trans. Antennas Propag.*, vol. 62, no. 8, pp. 4402–4407, Aug. 2014.

[3] ——, "Normalization-free chipless RFIDs by using dual-polarized interrogation," *IEEE Trans. Microw. Theory Techn.*, vol. 64, no. 1, pp. 310–318, Jan. 2016.

[4] S. Genovesi, F. Costa, A. Monorchio, and G. Manara, "Chipless RFID tag exploiting multifrequency delta-phase quantization encoding," *IEEE Antennas Wireless Propag. Lett.*, vol. 15, pp. 738–741, 2016.

[5] A. Vena, E. Perret, and S. Tedjni, "A depolarizing chipless RFID tag for robust detection and its FCC compliant UWB reading system," *IEEE Trans. Microw. Theory Techn.*, vol. 61, no. 8, pp. 2982–2994, Aug. 2013.

[6] M. Borgese, F. A. Dicandia, F. Costa, S. Genovesi, and G. Manara, "An inkjet printed chipless RFID sensor for wireless humidity monitoring," *IEEE Sensors J.*, vol. 17, no. 15, pp. 4699–4707, Aug. 2017.

[7] A. Lazaro, R. Villarino, F. Costa, S. Genovesi, A. Gentile, L. Buoncristiani, and D. Girbau, "Chipless dielectric constant sensor for structural health testing," *IEEE Sensors J.*, vol. 18, no. 13, pp. 5576–5585, Jul. 2018.

[8] A. M. J. Marindra and G. Y. Tian, "Chipless RFID sensor tag for metal crack detection and characterization," *IEEE Trans. Microw. Theory Techn.*, vol. 66, no. 5, pp. 2452–2462, May 2018.

[9] ——, "Multiresonance chipless RFID sensor tag for metal defect characterization using principal component analysis," *IEEE Sensors J.*, vol. 19, no. 18, pp. 8037–8046, Sep. 2019.

[10] V. Liu, A. Parks, V. Talla, S. Gollakota, D. Wetherall, and J. R. Smith, "Ambient backscatter: Wireless communication out of thin air," *ACM SIGCOMM Comput. Commun. Rev.*, vol. 43, no. 4, pp. 39–50, Aug. 2013.

[11] N. Van Huynh, D. T. Hoang, X. Lu, D. Niyato, P. Wang, and D. I. Kim, "Ambient backscatter communications: A contemporary survey," *Commun. Surveys Tuts.*, vol. 20, no. 4, pp. 2889–2922, Fourth quarter 2018.

[12] X. Lu, D. Niyato, H. Jiang, D. I. Kim, Y. Xiao, and Z. Han, "Ambient backscatter assisted wireless powered communications," *Wireless Commun.*, vol. 25, no. 2, pp. 170–177, Apr. 2018.

[13] P. R. Wiecha, A. Lecestre, N. Mallet, and G. Larrieu, "Pushing the limits of optical information storage using deep learning," *Nature Nanotechnol.*, vol. 14, no. 3, pp. 237–244, Mar. 2019.

[14] P. Kalansuriya, N. C. Karmakar, and E. Viterbo, "On the detection of frequency-spectra-based chipless RFID using UWB impulsed interrogation," *IEEE Trans. Microw. Theory Techn.*, vol. 60, no. 12, pp. 4187–4197, Dec. 2012.

[15] Z. Ruan and S. Fan, "Superscattering of light from subwavelength nanostructures," *Phys. Rev. Lett.*, vol. 105, no. 1, 013901, Jun. 2010.

[16] M. Gustafsson, K. Schab, L. Jelinek, and M. Capek, "Upper bounds on absorption and scattering," *New J. Phys.*, Mar. 2020, accepted for publication.

[17] I. Liberal, I. Ederra, R. Gonzalo, and R. W. Ziolkowski, "Upper bounds on scattering processes and metamaterial-inspired structures that reach them," *IEEE Trans. Antennas Propag.*, vol. 62, no. 12, pp. 6344–6353, Dec. 2014.

[18] O. D. Miller, C. W. Hsu, M. H. Reid, W. Qiu, B. G. DeLacy, J. D. Joannopoulos, M. Soljačić, and S. G. Johnson, "Fundamental limits to extinction by metallic nanoparticles," *Phys. Rev. Lett.*, vol. 112, no. 12, 123903, Mar. 2014.

[19] S. Molesky, P. Chao, W. Jin, and A. W. Rodriguez, "Global T operator bounds on electromagnetic scattering: Upper bounds on far-field cross sections," *Phys. Rev. Research*, vol. 2, no. 3, 033172, Jul. 2020.

[20] I. Liberal and R. W. Ziolkowski, "Analytical and equivalent circuit models to elucidate power balance in scattering problems," *IEEE Trans. Antennas Propag.*, vol. 61, no. 5, pp. 2714–2726, May 2013.

[21] I. Liberal, I. Ederra, R. Gonzalo, and R. W. Ziolkowski, "A multipolar analysis of near-field absorption and scattering processes," *IEEE Trans. Antennas Propag.*, vol. 61, no. 10, pp. 5184–5199, Oct. 2013.

[22] C. Sohl, M. Gustafsson, and G. Kristensson, "Physical limitations on broadband scattering by heterogeneous obstacles," *J. Phys. A: Math. Theor.*, vol. 40, no. 36, 11165, Aug. 2007.

[23] R. Fleury, J. Soric, and A. Alù, "Physical bounds on absorption and scattering for cloaked sensors," *Phys. Rev. B*, vol. 89, no. 4, 045122, Jan. 2014.

[24] J.-P. Hugonin, M. Besbes, and P. Ben-Abdallah, "Fundamental limits for light absorption and scattering induced by cooperative electromagnetic interactions," *Phys. Rev. B*, vol. 91, no. 18, 180202, May 2015.

[25] I. Liberal, I. Ederra, R. Gonzalo, and R. W. Ziolkowski, "Superbackscattering antenna arrays," *IEEE Trans. Antennas Propag.*, vol. 63, no. 5, pp. 2011–2021, May 2015.

[26] ——, "Superbackscattering from single dielectric particles," *J. Opt.*, vol. 17, no. 7, 072001, Jun. 2015.

[27] ——, "Superbackscattering nanoparticle dimers," *Nanotechnol.*, vol. 26, no. 27, 274001, Jun. 2015.

[28] C. A. Balanis, *Advanced Engineering Electromagnetics*. Hoboken, NJ: John Wiley & Sons, 2012.

[29] T. Hansen and A. D. Yaghjian, *Plane-Wave Theory of Time-Domain Fields: Near-Field Scanning Applications*. Hoboken, NJ: IEEE Press, 1999.

[30] C. F. Bohren and D. R. Huffman, *Absorption and Scattering of Light by Small Particles*. Hoboken, NJ: John Wiley & Sons, 2008.

[31] M. Born and E. Wolf, *Principles of Optics: Electromagnetic Theory of Propagation, Interference and Diffraction of Light*, 6th ed. Oxford, England: Pergamon Press, 2013.

[32] D. Torrungrueng, B. Ungan, and J. T. Johnson, "Optical theorem for electromagnetic scattering by a three-dimensional scatterer in the presence of a lossless half space," *IEEE Geosci. Remote Sens. Lett.*, vol. 1, no. 2, pp. 131–135, Apr. 2004.

[33] A. Small, J. Fung, and V. N. Manoharan, "Generalization of the optical theorem for light scattering from a particle at a planar interface," *J. Opt. Soc. Am. A*, vol. 30, no. 12, pp. 2519–2525, Dec. 2013.

[34] J. B. Andersen and A. Frandsen, "Absorption efficiency of receiving antennas," *IEEE Trans. Antennas Propag.*, vol. 53, no. 9, pp. 2843–289, Sep. 2005.

[35] P. Jin and R. W. Ziolkowski, "Metamaterial-inspired, electrically small Huygens sources," *IEEE Antennas Wireless Propag. Lett.*, vol. 9, pp. 501–505, May 2010.

[36] D.-H. Kwon, "On the radiation Q and the gain of crossed electric and magnetic dipole moments," *IEEE Trans. Antennas Propag.*, vol. 53, no. 5, pp. 1681–1687, May 2005.

[37] P. Alitalo, A. Karilainen, T. Niemi, C. Simovski, and S. Tretyakov, "Design and realisation of an electrically small Huygens source for circular polarisation," *IET Microw. Antennas Propag.*, vol. 5, no. 7, pp. 783–789, May 2011.

[38] M.-C. Tang, H. Wang, and R. W. Ziolkowski, "Design and testing of simple, electrically small, low-profile, Huygens source antennas with broadside radiation performance," *IEEE Trans. Antennas Propag.*, vol. 64, no. 11, pp. 4607–4617, Nov. 2016.

[39] M.-C. Tang, T. Shi, and R. W. Ziolkowski, "Electrically small, broadside radiating Huygens source antenna augmented with internal non-Foster elements to increase its bandwidth," *IEEE Antennas Wireless Propag. Lett.*, vol. 16, pp. 712–715, 2017.

[40] M.-C. Tang, B. Zhou, and R. W. Ziolkowski, "Low-profile, electrically small, Huygens source antenna with pattern-reconfigurability that covers the entire azimuthal plane," *IEEE Trans. Antennas Propag.*, vol. 65, no. 3, pp. 1063–1072, Mar. 2017.

[41] R. W. Ziolkowski, "Custom-designed electrically small Huygens dipole antennas achieve efficient, directive emissions into air when mounted on a high permittivity block," *IEEE Access*, vol. 7, pp. 163 365–163 383, Nov. 2019.

[42] W. Lin and R. W. Ziolkowski, "Electrically small Huygens antenna-based fully-integrated wireless power transfer and communication system," *IEEE Access*, vol. 7, pp. 39 762–39 769, Mar. 2019.

[43] M. Gustafsson and M. Capek, "Maximum gain, effective area, and directivity," *IEEE Trans. Antennas Propag.*, vol. 67, no. 8, pp. 5282–5293, Aug. 2019.

[44] S. Mikki, S. Clauzier, and Y. Antar, "A correlation theory of antenna directivity with applications to superdirective arrays," *IEEE Antennas Wireless Propag. Lett.*, vol. 18, no. 5, pp. 811–815, May 2019.

[45] A. I. Uzkov, "An approach to the problem of optimum directive antennae design," *Comptes Rendus (Doklady) de l'Academie des Sciences de l'URSS*, vol. 53, pp. 35–38, 1946.

[46] R. C. Hansen, *Electrically Small, Superdirective, and Superconducting Antennas*. Hoboken, NJ: John Wiley & Sons, 2006.

[47] A. T. Parsons, "Maximum directivity proof for three-dimensional arrays," *J. Acoust. Soc. Am.*, vol. 82, no. 1, pp. 179–182, Jul. 1987.

[48] E. E. Altshuler, T. H. O'Donnell, A. D. Yaghjian, and S. R. Best, "A monopole superdirective array," *IEEE Trans. Antennas Propag.*, vol. 53, no. 8, pp. 2653–2661, Aug. 2005.

[49] A. D. Yaghjian, T. H. O'Donnell, E. E. Altshuler, and S. R. Best, "Electrically small supergain end-fire arrays," *Radio Sci.*, vol. 43, no. 3, RS3002, Jun. 2008.

[50] O. S. Kim, S. Pivnenko, and O. Breinbjerg, "Superdirective magnetic dipole array as a first-order probe for spherical near-field antenna measurements," *IEEE Trans. Antennas Propag.*, vol. 60, no. 10, pp. 4670–4676, Oct. 2012.

[51] T. Kokkinos and A. P. Feresidis, "Electrically small superdirective endfire arrays of metamaterial-inspired low-profile monopoles," *IEEE Antennas Wireless Propag. Lett.*, vol. 11, pp. 568–571, May 2012.

[52] A. Haskou, A. Sharaiha, and S. Collardey, "Design of small parasitic loaded superdirective end-fire antenna arrays," *IEEE Trans. Antennas Propag.*, vol. 63, no. 12, pp. 5456–5464, Dec. 2015.

[53] A. Clemente, M. Pigeon, L. Rudant, and C. Delaveaud, "Design of a super directive four-element compact antenna array using spherical wave expansion," *IEEE Trans. Antennas Propag.*, vol. 63, no. 11, pp. 4715–4722, Nov. 2015.